CHEMISTRY OF MATERIALS

pubs.acs.org/cm Article

Electronic Tuning of Active Sites in Bifunctional Covalent Organic Frameworks for Photoassisted CO_2 Electrocatalytic Full Reaction

Huimin Ding, Yi-Rong Wang, Ming Liu, Jing-Wen Shi, Tao-Yuan Yu, Yuan-Sheng Xia, Meng Lu, Yi-Lu Yang, Yifa Chen,* Shun-Li Li, and Ya-Qian Lan*

Cite This: *Chem. Mater.* 2022, 34, 10752−10760 Read Online

ABSTRACT: Realizing simultaneously energy-efficiency improvement and green economic implementation remains a daunting challenge in addressing the low-efficiency issues of CO_2 electroreduction to meet the sustainable development strategy. Here, we propose a series of porphyrin-based COFs (**TTCOF-M, M = Co, Ni**, and **Cu**) as model catalysts to study the hybrid CO_2 electrocatalytic full reaction for the first time, during which the catalysts can simultaneously accomplish photoassisted CO_2 electroreduction and 4-nitrophenol (4-NP) mineralization. As model catalysts, the effects of various parameters have been intensively studied from typical tandem electro-reactions to extended photoassisted ones. Specifically, **TTCOF-Co** can achieve the cathodic reduction efficiency increasing from 90 to 96% (−0.7 V) after illumination and simultaneously 5 times shortened reaction time with a 4-NP degradation efficiency of ∼99%. Notably, the 4-NP mineralization rate is calculated to be ∼93.51% with ∼30.27 mmol/g/h CO_2 production rate, and a rarely investigated mechanism relating to the 4-NP electro-degradation has been intensively studied.

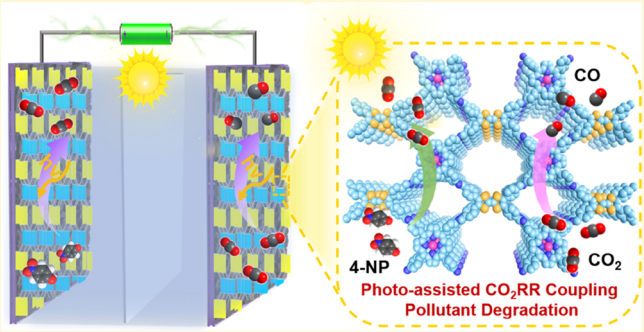

■ INTRODUCTION

With the widespread use of pesticides, drugs, dyes, and other organic substances, the wastewater pollution caused by the discharge of more and more harmful pollutants is becoming increasingly serious.[1,2] Currently, phenolic contaminants (e.g., phenol, cresol, nitrophenol or nitro-cresol, etc.) in wastewater have caused prominent problems to the ecosystem or human beings and remain as a hot topic.[3,4] Among them, nitrophenol-based contaminates are a class of notorious organic compounds with obvious toxicity and hard biodegradability, yet they are continuously used as drugs, synthetic dyes, and pesticides in industry, causing giant damage to human health through erosion of the liver, kidney, central nervous system, and blood system.[5,6] For instance, 4-nitrophenol (4-NP) as a common nitrophenol-based contaminant with stable chemical properties and high toxicity, possessing high threat to microorganisms and humans, has facilitated the U.S. Environmental Protection Agency (USEPA) to declare 4-NP as a priority pollutant and limited its permissible concentration range to 1∼20 ppb.[7] Aiming at this target, traditional removal methods, such as adsorption,[8] filtration,[9] microbial degradation,[10] or advanced oxidation process (AOP),[11,12] have been studied for phenolic contaminant treatment, yet most of which still face challenges like low selectivity/energy efficiency or toxic byproducts, etc., which will in turn increase the costs and power supply during these processes. In this regard, it would be much desired to seek economy and energy benign treatment methods to rationally remove nitrophenol contaminants like 4-NP from wastewater and maximize resource utilization.[13,14]

From the perspective of sustainable chemistry and carbon neutrality, the electrocatalytic carbon dioxide reduction reaction (CO_2RR) is an emerging and promising green technology path that can use electrical energy to convert CO_2 into valuable fuels and fine chemicals (e.g., CO, CH_4, HCOOH, C_2H_4, etc.).[15−21] However, the oxygen evolution reaction (OER) in the anode, counting ∼90% of the total energy of the system, has caused bottlenecks like high energy consumption or low overall energy conversion efficiency.[22−26] In this regard, in addition to the design of powerful electrocatalysts,[27−29] it would be much essential to systematically study the CO_2RR devices/systems or develop new electrochemical processes to maximize energy utilization.[30] To this end, much attention has been paid to explore suitable anodic reactions to be coupled with CO_2RR, for example,

Received: September 28, 2022
Revised: November 22, 2022
Published: December 2, 2022

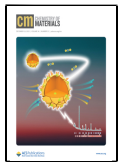

https://doi.org/10.1021/acs.chemmater.2c02962
Chem. Mater. 2022, 34, 10752−10760

electro-degradation of nitrophenol contaminants.[31,32] During past decades, some pioneering studies have applied Co_3O_4@ Cl||SnO_2/CC or Co_3O_4@Cl||CuO electrodes to study the possibility of CO_2 electroreduction coupling 4-NP electro-degradation.[33−35] However, this field is still at the early stage and there are some unresolved issues to be addressed: (1) the catalysts for the anode and cathode sides need diverse functions, which would require different catalysts and in turn enhance the cost or complexity in catalyst design; (2) the mechanism study is still rare for the reported studies, especially for the electro-degradation of pollutants, and (3) other green energy forms (e.g., light or microwave energy)[36,37] that could assist the tandem catalysis to achieve higher efficiency have been rarely explored. Especially for the photoassisted tandem system,[38−40] the application of green light energy might be much favorable to improve the efficiency or save the energy consumption of the tandem system. Thus, it would be much desired to explore powerful electrocatalysts that can achieve simultaneous value-added product generation and high-efficient nitrophenol contaminant removal, yet the required multifunctionality of photo/electrocatalysts for such systems further accelerates the difficulty in catalyst design.[41,42]

Covalent organic frameworks (COFs), a kind of famous porous crystalline frameworks that are constructed from periodically connected organic monomers by covalent bonds,[43−45] have received widespread attention in the fields of electro-/photocatalysis, sensing, gas storage/separation, energy storage, etc. With the inert high crystallinity and stability, large specific surface area, and small density, COFs are notable materials with tunable functionality originating from their molecularly designable constructs.[46−48] During past decades, COFs, especially that with metalloporphyrin or metallophthalocyanine counterparts, have been proven to be potential catalysts for the electrocatalytic CO_2RR in the generation of products like CO, HCOOH, CH_4 or C_2H_4, etc.[49−52] Based on this, they might be desired candidates for the extended photoassisted CO_2 electroreduction coupling pollutant degradation owing to their superiority in flexible structure design that might fulfill the multirequirements (e.g., photo-sensitivity or electro-activity[38]) of this powerful system. Therefore, we intend to study the possibility of COF-based catalysts as the bifunctional electrode catalysts with both photo-sensitive and electro-active units to explore the photo-assisted CO_2 electroreduction coupling pollutant degradation, yet the applications of COFs in such systems have been rarely reported and remain a hot topic with daunting challenges to be explored.

In this work, it is proposed for the first time that we apply a series of porphyrin-based COFs (**TTCOF-M, M = Co, Ni, and Cu**) with tunable active sites as model catalysts to study the photoassisted CO_2 electroreduction coupling 4-NP degradation (DNP or $D_{4\text{-NP}}$), during which they serve as the bifunctional electrodes that can simultaneously accomplish the efficient CO_2 electroreduction and 4-NP mineralization in an integrated system (Scheme 1). As model catalysts, the effects of various parameters have been intensively studied from typical tandem electro-reactions to extended photo-assisted ones. Best of them, **TTCOF-Co** can achieve the cathodic reduction efficiency increasing from 90% to 96% (−0.7 V) after illumination and simultaneously 5 times shortened reaction time with a 4-NP degradation efficiency of ∼99%. Moreover, the rarely investigated mechanism relating to the 4-NP electro-degradation has been intensively studied

Scheme 1. Schematic Representation of TTCOF-M (M = Co, Ni, and Cu) in the Photoassisted CO_2 Electroreduction Coupling 4-NP Degradation (Denoted As DNP or $D_{4\text{-NP}}$)

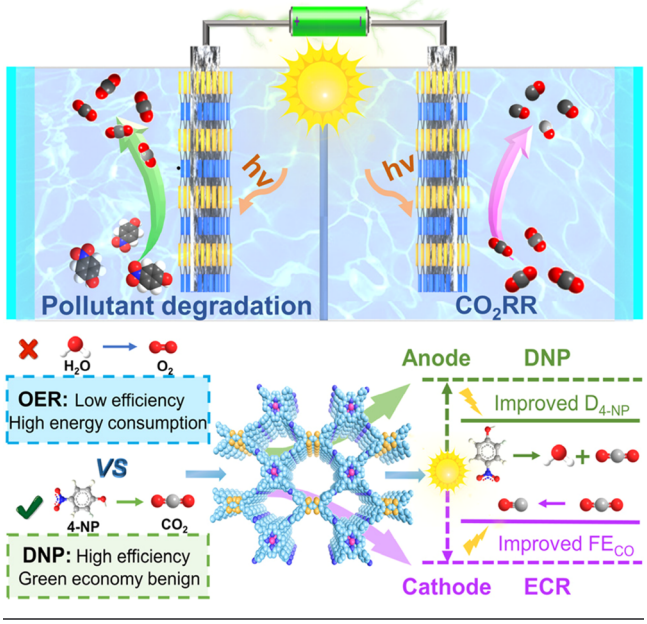

with density functional theory (DFT) calculations and various characterizations. This work paves a new way in proposing porous crystalline catalysts for photoassisted tandem catalysis systems, which might facilitate the potential industrial process of electrocatalytic CO_2RR in extended fields like environment remediation.

■ RESULTS AND DISCUSSION

TTCOF-M (M = Co, Ni, and Cu) are synthesized by the solvothermal method and characterized to accomplish photo-assisted tandem catalysis.[53,54] In the structure of **TTCOF-Co**, the covalent connection between 2,3,6,7-tetra (4-formylphenyl)-tetrathiafulvalene (TTF-4CHO) and metallized tetra-(4-aminophenyl) porphyrin group (**TAPP-Co**) produces a dual-channel pore structure with pore sizes of ∼1.10 nm and ∼1.57 nm and the distance between the stack layers is ∼3.69 Å (Figure 1a).[55] The powder X-ray diffraction (PXRD) pattern confirms that the synthesized **TTCOF-Co** has good crystallinity, which corresponds to the theoretical simulated pattern (Figure 1b). The structure of **TTCOF-Co** is modeled in the P21 space group, and the unit cell parameters are further refined from the PXRD pattern through Pawley fitting. Based on previously reported studies, the theoretical PXRD pattern obtained in this way matches well with the experimental result (Figure 1b).[55,56] For **TTCOF-Ni** and **TTCOF-Cu**, they present iso-reticular structures and similar PXRD patterns as that of **TTCOF-Co** (Figure S1). In addition, the Fourier transform infrared (FT-IR) spectral measurements are performed to support the chemical structures of **TTCOF-M (M = Co, Ni, and Cu)**. The peak at ∼1622 cm^{-1} confirms the successful formation of C═N bonds in the structure. Besides, the N−H in-plane vibration at 964 cm^{-1} is significantly changed, and a new absorption peak appears at 999 cm^{-1} when compared with TAPP, indicating that metal coordination occurred in the porphyrin center (Figure S2). In addition, the X-ray photoelectron spectroscopy (XPS) tests are carried out to determine the surface electronic state and the metal valence

https://doi.org/10.1021/acs.chemmater.2c02962
Chem. Mater. 2022, 34, 10752−10760

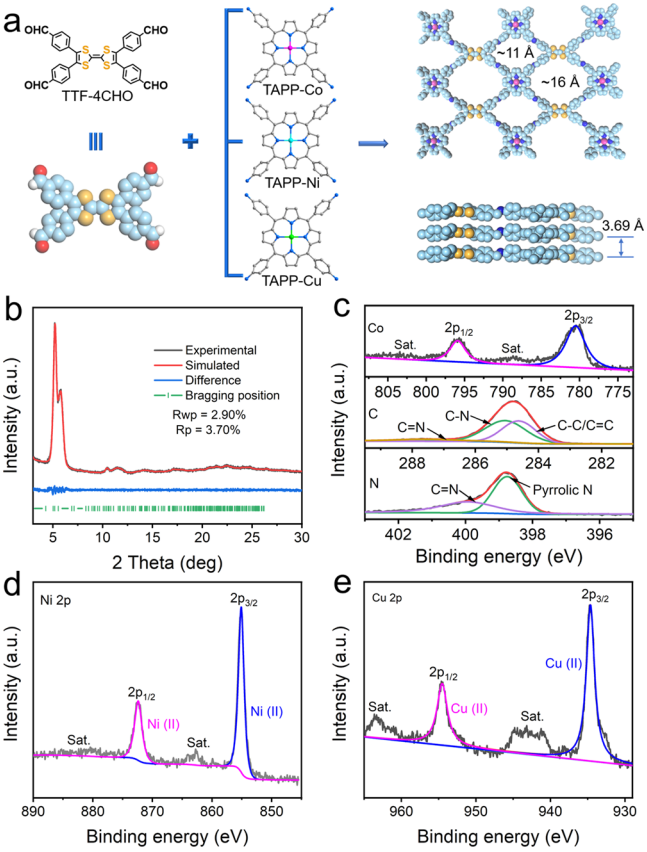

Figure 1. Structure and characterization of **TTCOF-M** (**M** = **Co**, **Ni**, and **Cu**). (a) Structure of **TTCOF-M** obtained through the condensation of TTF-4CHO and TAPP-M. (b) Experimental (black line) and simulated (red line) PXRD patterns of **TTCOF-Co**. (c) XPS spectrum of **TTCOF-Co**: Co 2p, C 1s, and N 1s. (d) High-resolution Ni 2p XPS profiles of **TTCOF-Ni**. (e) High-resolution Cu 2p XPS profiles of **TTCOF-Cu**.

state of **TTCOF-M** (Figures S3, S4, and S5). The results show the existence of N═C bonds in **TTCOF-Co**, as displayed in the N 1s and C 1s spectra (Figure 1c).[57,58] The observed Co $2p_{3/2}$ binding energy of 780.68 eV and the $2p_{1/2}$ binding energy of 795.93 eV are ascribed to Co(II) (Figure 1c). Similarly, the XPS result suggests that the metal centers in **TTCOF-Ni** and **TTCOF-Cu** are all bivalent states (Figure 1d,e).

The two-dimensional layered porous structure produced by the assembly of metalloporphyrin and TTF might be conducive to the mass transfer of substrates and the enrichment of CO_2. The porosity of **TTCOF-M** (**M** = **Co**, **Ni**, and **Cu**) has been evaluated by N_2 sorption tests at 77 K after solvent exchange with tetrahydrofuran and activation of the COF under vacuum at 120 °C. The N_2 isotherm curves present a characteristic Type I shape, which reveals the presence of micropores for **TTCOF-M** (**M** = **Co**, **Ni**, and **Cu**) (Figure S6a). The Brunauer−Emmett−Teller specific surface area (S_{BET}) and the total pore volume (V_t) of **TTCOF-Co** are calculated to be 400.02 $cm^2\ g^{-1}$ and 0.575 $cm^3\ g^{-1}$ (Figure S6), respectively. As a comparison, the S_{BET} and V_t of **TTCOF-Ni** (406.92 $cm^2\ g^{-1}$ and 0.659 $cm^3\ g^{-1}$) and **TTCOF-Cu** (316.28 $cm^2\ g^{-1}$ and 0.442 $cm^3\ g^{-1}$) are close to those of **TTCOF-Co** with a slight difference (Figures S7 and S8). For the pore size distributions of TTCOF-M (M = Co, Ni, and Cu), the pore width at ∼1.1 nm can be mainly detected for all of them, which are in good agreement with the calculated pore structures. However, there exists minor defective pore distribution for the pore width centered at ∼1.6 nm, which makes it to be a relatively broad distribution and might be possibly attributed to the defects generated in their nanostructures (Figures S7b and S8b).[55] Moreover, the CO_2 adsorption tests of **TTCOF-M** (**M** = **Co**, **Ni**, and **Cu**) are further carried out. The CO_2 adsorption capacity values of **TTCOF-Co** are 54.30 and 30.40 $cm^3\ g^{-1}$ at 273 K and 298 K (Figure S9), respectively, which are higher than those of **TTCOF-Ni** (51.43 $cm^3\ g^{-1}$, 273 K and 28.67 $cm^3\ g^{-1}$, 298 K) and **TTCOF-Cu** (35.72 $cm^3\ g^{-1}$, 273 K and 19.88 $cm^3\ g^{-1}$, 298 K) (Figures S10 and S11). Furthermore, the stability tests as certified by the PXRD patterns show that **TTCOF-Co** can still maintain the original crystal structure after soaking in 0.5 M $KHCO_3$ and 0.1 M Na_2SO_4 solutions for 5 days, indicating high chemical stability (Figure S12). These results provide a basis for further study of photoassisted CO_2 electroreduction coupling pollutant degradation.

In addition, the morphology of **TTCOF-M** (**M** = **Co**, **Ni**, and **Cu**) has been studied by the scanning electron microscopy (SEM) and transmission electron microscopy (TEM) tests. The SEM images indicate that **TTCOF-Co** is a kind of rectangular nanoparticles with a size of ∼150 nm (Figure S13a), which is different from **TTCOF-Ni** (nanosheets, ∼100 nm) (Figure S14a) and **TTCOF-Cu** (hollow balls, ∼500 nm) (Figure S15a). The morphology is also confirmed by the TEM image (Figures S13b, S14b, and S15b). Moreover, the high-resolution transmission electron microscopy (HR-TEM) image also demonstrates that **TTCOF-Co** has a highly ordered aperture, and clear directional lattice stripes can be observed with a lattice spacing of 1.18 nm (ascribing to the (110) crystalline plane),[55] confirming the high crystallinity of the resulting **TTCOF-Co** (Figures S13b, S14b, and S15b). The corresponding energy dispersive spectrometry (EDS) mapping images demonstrate that C, N, S, and Co elements are evenly distributed in the rectangular nanoparticles (Figures S16 and S19a). In addition, C, N, S, and Ni are uniformly distributed over TTCOF-Ni (Figures S17 and S19b). The element distribution of TTCOF-Cu is similar (Figures S18 and S19c). For **TTCOF-Co**, the total content of Co measured by inductively coupled plasma optical emission spectroscopy (ICP-OES) is 4.31 wt %, which matches well with the EDS test (the content of Co is 4.3 wt %) (Table S1). Ultraviolet photoelectron spectroscopy (UPS) is conducted to determine the electronic properties of **TTCOF-M** (**M** = **Co**, **Ni**, and **Cu**) (Figures S20, S21, and S22), showing their high photosensitivity. In addition, they have a wide range of visible light absorption in the solid-state UV tests, which might fulfill the requirements of **TTCOF-M** (**M** = **Co**, **Ni**, and **Cu**) and serve as potential candidates for further performance tests (Figure S23).

Based on the above characterization, we further take advantage of **TTCOF-M** (**M** = **Co**, **Ni**, and **Cu**) as the model catalysts to explore the photoassisted CO_2 electroreduction coupling pollutant degradation, which can realize the synchronous completion of green treatment of wastewater pollutants and rational utilization of energy. We exploit a simple and common device, namely, H-type electrolytic cell, in which CO_2RR is carried out at the cathode and 4-NP degradation is introduced at the anode to be coupled with CO_2RR to improve the economic feasibility and the total energy utilization. The properties of the electrocatalytic CO_2

https://doi.org/10.1021/acs.chemmater.2c02962
Chem. Mater. 2022, 34, 10752−10760

reduction and 4-NP electrocatalysis degradation processes are explored at room temperature (∼25 °C); Pt foil and Ag/AgCl electrodes are used as the counter electrode and reference electrodes, respectively.

To accomplish the design concept, the CO_2 electroreduction performances of **TTCOF-M** (**M = Co, Ni,** and **Cu**) at the cathodic side are first studied. Taking **TTCOF-Co** as an example, the current density at different potentials under Ar and CO_2 atmospheres is analyzed by linear scanning voltammetry (LSV) (Figure 2a). The current density under

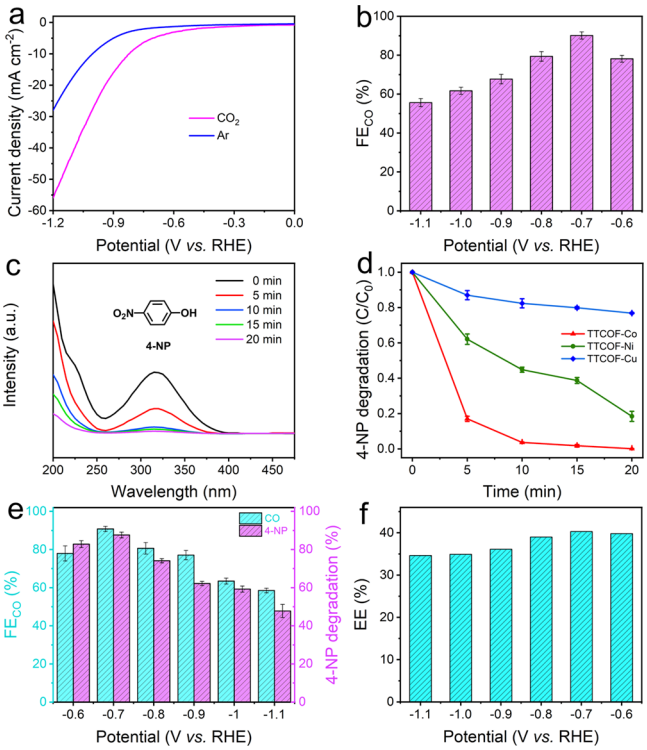

Figure 2. Electrocatalytic performance of **TTCOF-M** (**M = Co, Ni,** and **Cu**). (a) Linear sweep voltammetry curves of the cathode. (b) Faradaic efficiency of CO at different potentials for **TTCOF-Co**. (c) Absorbance intensity for 4-NP by electrocatalysis of **TTCOF-Co** under different times. (d) Degradation for 4-NP in different times of **TTCOF-M** (**M = Co, Ni,** and **Cu**) at −0.7 V vs RHE. (e) Performance of CO_2 electroreduction coupling pollutant degradation by **TTCOF-Co** at different potentials. (f) Total energy efficiency of CO_2 electroreduction coupling pollutant degradation for **TTCOF-Co**.

the CO_2 atmosphere is obviously higher than that under the Ar atmosphere, which implies that **TTCOF-Co** has high catalytic activity in the electrocatalytic CO_2RR. To further investigate the selectivity of the catalyst in the CO_2RR process, electrolytic reduction tests are carried out at selected potentials (−0.6 to −1.1 V vs RHE) (Figure 2b). The gas reduction products of CO_2RR are detected and analyzed by gas chromatography (GC). It is found that the CO_2 is mainly reduced to CO and H_2, and the sum of gaseous products under each potential is ∼100% (Figure S24). ^{1}H NMR spectroscopy displays that the liquid products are negligible under the optimal test conditions (Figure S25).

For **TTCOF-Co**, it exhibits the highest FE_{CO} value of 90.14 ± 1.80% at −0.7 V, which is much superior to that of **TTCOF-Cu** (<5%) and **TTCOF-Ni** (∼22%, −0.9 V) (Figures S26 and S27). To verify the carbon source of the reduction gas products, the isotopic-labeling experiment that uses $^{13}CO_2$ as the substrate is conducted under identical reaction conditions and the products are analyzed by GC−MS. The peak at m/z = 29 is assigned to ^{13}CO, demonstrating that the carbon sources of reduction gas products come from the CO_2 conversion (Figure S28). Blank carbon paper is tested at the cathode using the same test condition, and it shows no catalytic activity of CO_2RR (Figure S29). For the anodic side, the degradation ability of different model catalyst **TTCOF-M** (**M = Co, Ni,** and **Cu**) in the tandem CO_2 electroreduction coupling 4-NP degradation system has been evaluated. According to the liquid UV absorption curve, it can be seen that the absorbance intensity of 4-NP at 337 nm gradually weakens with the prolongation of degradation time, and the ultraviolet absorption intensity finally approaches 0 at 20 min. Additionally, the color of the 4-NP solution gradually becomes lighter during the experiment progress, and finally approaches a colorless state within 20 min under the best condition (Figure 2c). The degradation rate curves show that **TTCOF-Co** possesses the highest degradation ability, and its degradation efficiency is 99.8 ± 0.11% at −0.7 V in 20 min, which is higher than that of **TTCOF-Ni** (80.71% ± 2.84%) and **TTCOF-Cu** (22.94 ± 0.41%) (Figure 2d). Besides, the degradation efficiency of 4-NP by the photocatalytic process alone is not significant (<10%, 20 min), implying that it is the electrocatalysis-dominated process (Figure S30). In addition, after the control test, it is found that blank carbon paper has no effect on 4-NP degradation under electrocatalysis and photocatalysis conditions (Figures S31 and S32).

Specifically, in the tandem process, the products from the anode and cathode are separately collected and the FEs are calculated after passing 5 C charges. In detail, for **TTCOF-Co** as the anode and cathode, CO_2 can be transformed into CO at the cathode with FE_{CO} of nearly 77.01 ± 3.96% at −0.6 V and reach up to the maximum value of 90.02 ± 1.34% at −0.7 V (Figure 2e). Meanwhile, the corresponding degradation efficiency of 4-NP at the anode can reach up to 83.0 ± 1.81% at −0.6 V and a maximum value of 88.01 ± 1.49% at −0.7 V after passing 5 C charges. With the increase of potential, the reduction efficiency of CO_2 and the degradation efficiency of 4-NP are gradually decreased (Figure 2e). In contrast, when **TTCOF-Ni** is applied as the anode and cathode, the degradation efficiency of 4-NP at the anode can reach up to 92.61 ± 0.9% at −0.8 V, while the corresponding FE_{CO} is only 23.65 ± 1.09% (Figure S33). For **TTCOF-Cu**, it has negligible CO_2RR performance for the cathode side and ∼20% 4-NP degradation rate for the anode side in the tandem process. These results imply that the **TTCOF-Co** could be utilized as the efficient electrocatalyst for CO_2 electroreduction coupling 4-NP degradation. Furthermore, to reveal the electrocatalytic kinetics on the electrode/electrolyte surface of **TTCOF-M** during the electrochemical CO_2RR and 4-NP degradation process, the electrochemical impedance spectroscopy (EIS) tests of the three samples are conducted (Figure S34). As shown in the Nyquist plots, **TTCOF-Co** exhibits smaller charge transfer resistance than that of **TTCOF-Ni** and **TTCOF-Cu**, suggesting that **TTCOF-Co** can provide faster electron transfer from the catalyst surface to the reactant in intermediate generation, thus enhancing the catalytic activity (Figure S34). In addition, the EE of **TTCOF-Co** is also calculated to evaluate the energy conversion efficiency of CO_2 electroreduction coupling pollutant degradation and the result

https://doi.org/10.1021/acs.chemmater.2c02962
Chem. Mater. 2022, 34, 10752−10760

displays that **TTCOF-Co** can reach up to a maximum value of 40.31% at −0.7 V (Figure 2f).[59]

During past years, some pioneering studies have proven that photoassisted electrocatalysis is a promising strategy to further enhance the CO_2 conversion efficiency in electrocatalytic CO_2RR.[38] Thus, we hypothesized that light irradiation might probably facilitate the CO_2 electroreduction coupling 4-NP degradation. To verify it, the LSV tests of tandem CO_2RR and 4-NP degradation with or without light irradiation have been conducted. It shows that **TTCOF-Co** has a higher current density under the light condition than that under the dark one (Figure 3a). In addition, the current density increases

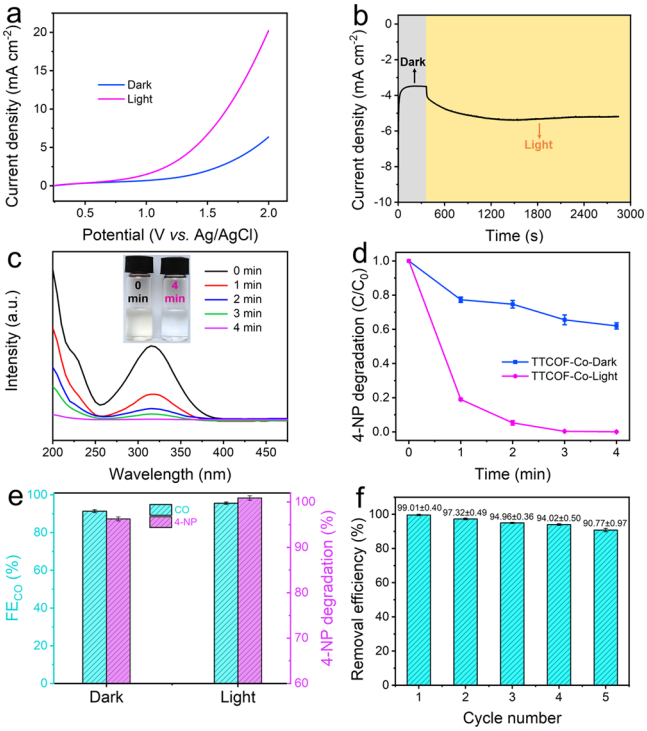

Figure 3. Performance of **TTCOF-Co** for photoassisted tandem CO_2RR and 4-NP degradation. (a) Linear sweep voltammetry curves of the anode. (b) Stability of **TTCOF-Co** in the dark and light. (c) Absorbance intensity of 4-NP for photoelectric coupling under different times. (d) Degradation of 4-NP under dark and light conditions. (e) Performance comparison of the anode and cathode under −0.7 V with or without light irradiation. (f) Recycling performance of **TTCOF-Co** for 4-NP degradation under light irradiation.

obviously with the assistance of irradiation, as revealed by the chronoamperometry test, which provides a good test basis for the photoassisted tandem CO_2RR and 4-NP degradation investigation (Figure 3b). Then, the photoassisted tandem CO_2RR and 4-NP degradation tests are subsequently carried out. For the anode side, the absorption intensity decreases rapidly in the ultraviolet absorption spectrum and the color of the solution becomes nearly colorless within 4 min with the degradation efficiency of 4-NP reaching up to 99% (Figure 3c), which is ∼5 times shortened in the time when compared with that without light irradiation (Figure 3c,d). Meanwhile, the FE_{CO} of the CO_2RR process at the cathode is also improved from 90.02 ± 1.34 to 96.22 ± 0.60% at −0.7 V under light irradiation, indicating that the 4-NP degradation and CO_2RR performances are highly improved with the assistance of light energy (Figure 3e). In comparison, for **TTCOF-Ni**, the degradation efficiency of 4-NP at the anode can reach up to 97.45 ± 1.53% at −0.8 V while the corresponding FE_{CO} is only 26.07%, which has a slight improvement under light irradiation (Figure S35). These results imply that **TTCOF-Co** could be utilized as an efficient electrocatalyst for photoassisted tandem 4-NP degradation and CO_2RR. In addition, recyclability is a crucial parameter for evaluating the durability properties of catalysts for further applications. **TTCOF-Co** with the optimal catalytic performance of photoassisted tandem CO_2RR and 4-NP degradation is selected to investigate the recycle experiment. After catalysis, the recovered **TTCOF-Co** electrode can be reused in repetitive reactions with negligible loss of its high catalytic performance for five cycles (Figure 3f), further proved by the ICP leaching test; negligible leaching metal ions are detected in the anode and cathode solution, demonstrating that **TTCOF-Co** has excellent stability in the photoassisted tandem CO_2RR and 4-NP degradation process (Table S2). Additionally, the structural integrity of **TTCOF-Co** remains intact after five catalysis cycles, as proved by the PXRD tests, indicating the high stability of **TTCOF-Co** (Figure S36).

Reactive species like •OH and $O_2^{\bullet-}$ play key roles in the oxidation of organic contaminants for organic pollutant degradation as proposed by the reported literature.[60−62] To provide direct evidence for the presence of reactive species, 5,5-dimethyl-1-pyrroline N-oxide (DMPO)-trapped electron paramagnetic resonance (EPR) experiments are carried out. The characteristic signal of EPR is not detected under dark conditions, while the characteristic peak of $O_2^{\bullet-}$ is observed under light irradiation. In addition, DMPO-•OH is also captured through the characteristic peak (Figure S37).[62] These EPR results clearly show that •OH and $O_2^{\bullet-}$ are generated on **TTCOF-Co** during the degradation process. Also, under light irradiation, the intensity of the EPR signal value of •OH is enhanced, which means that the amount of •OH generated increases and the degradation reaction rate is accelerated (Figure 4a). Similarly, combined with the EPR test results, TTCOF-Ni can also produce a certain amount of •OH to degrade 4-NP under the same conditions above mentioned (Figure S38). To better understand the mechanism of 4-NP degradation, more experiments have been conducted. According to the high-performance liquid chromatography (HPLC) results, the main intermediate 1,4-benzoquinone (*BQ) is detected during the degradation process (Figure 4b). Besides, the generated intermediate can be mainly mineralized to CO_2 and H_2O by the deep oxidation as revealed by the GC results. The 4-NP mineralization rate is 93.51% ± 2.5% with the amount of CO_2 produced that reaches up to ∼30.27 mmol g^{-1} h^{-1}. The total organic carbon content after the degradation reaction is approximately the same as the content of C in the initial 4-NP before the degradation of **TTCOF-Co**. Based on the promising results, if a sufficient amount of 4-NP can be mineralized in a closed-loop photoassisted tandem system as described above, the generated CO_2 can be utilized as the carrier substrate to be converted into higher value-added products at the cathode side, thus accomplishing the efficient transfer from organic pollutants to valuable products.

Furthermore, we propose the possible degradation pathway of 4-NP according to the abovementioned results and reported literature (Figure S39)[63] and evaluate the superiority and application of the **TTCOF-M** system. In general, based on the previously reported steps, 4-NP is first converted into 4-nitrosophenol (*PNSP) and 4-aminophenol (*PAP). Then,

https://doi.org/10.1021/acs.chemmater.2c02962
Chem. Mater. 2022, 34, 10752−10760

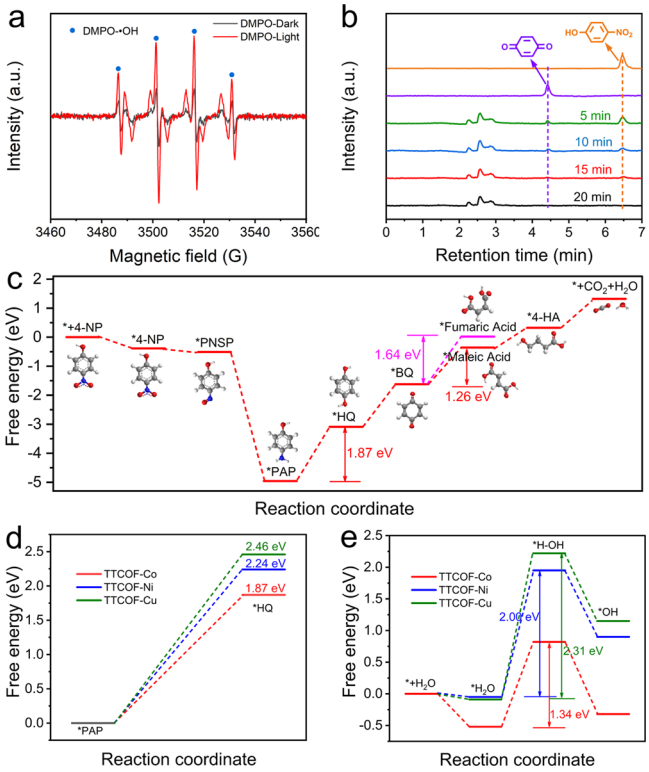

Figure 4. 4-NP degradation process. (a) Intensity of the EPR signal value of •OH before and after light irradiation. (b) Liquid product detection. (c) Gibbs free energy change diagrams of the 4-NP degradation process. (d) Gibbs free energy change diagrams of the *PAP to *HQ process on **TTCOF-Co**, **TTCOF-Ni**, and **TTCOF-Cu**. (e) Gibbs free energy change diagrams of the •OH generate process on **TTCOF-Co**, **TTCOF-Ni**, and **TTCOF-Cu**.

the •OH can attack the hydroxyl group counter position of 4-NP to generate 4-hydroxyphenol (*HQ), and then, *BQ is produced via the fast electron shuttle mechanism existence between *HQ and *BQ. After that, the *HQ and *BQ are further converted into ring-opening products of fumaric acid (*FA) or maleic acid (*MA) under the action of •OH and $O_2^{\bullet-}$. The ring-opening product is then completely degraded and will eventually mineralize into CO_2 and H_2O (Figure S39). In order to better understand the mechanism of catalytic degradation, DFT calculations are carried out to reveal the detailed free energy diagram for each reaction coordinate during the 4-NP degradation pathway on **TTCOF-Co**.[64−66] The formation of the *HQ intermediate is the rate-determining step in the 4-NP degradation reaction process, and the reaction energy barrier is 1.87 eV. In addition, the calculated results show that the energy barrier for the generation of fumaric acid (ΔG = 1.26 eV) is lower than that of maleic acid (ΔG = 1.64 eV). Therefore, the *BQ is more inclined to generate FA and further be mineralized to CO_2 and H_2O by deep oxidation (Figures 4c and S40). Then, the reaction pathway of *PAP to *HQ is further calculated by replacing the Co in the porphyrin center with Ni and Cu (Figures S41 and S42). Interestingly, as revealed by DFT calculation results, the energy barrier for the generation of *HQ on **TTCOF-Ni** (ΔG = 2.24 eV) and **TTCOF-Cu** (ΔG = 2.46 eV) is higher than that of **TTCOF-Co** (ΔG = 1.87 eV), which is consistent with the experimental results (Figure 4d). Based on the previous exploration, •OH plays a major role in the degradation process. Thus, we further explore the pathway of the generation of •OH (Figure S43). For the three catalysts, the rate-determining step in the reaction process of generating •OH is the decomposition of *H_2O into *H-OH (Figures S44 and S45). The rate-limiting step energy barrier of **TTCOF-Co** is 1.34 eV, which is lower than that of **TTCOF-Ni** (ΔG = 2.00 eV) and **TTCOF-Cu** (ΔG = 2.31 eV) (Figure 4e), indicating the highest activity of **TTCOF-Co** for the 4-NP degradation process.

Therefore, we propose a possible electrochemical degradation pathway from 4-NP to CO_2 to better understand the catalytic degradation process. Under the effect of •OH, 4-NP is activated to produce a series of intermediates and the *PAP generating *HQ is the rate-determining step. For **TTCOF-M (M = Co, Ni, and Cu)**, **TTCOF-Co** with Co-TAPP as the active center has the highest activity for the generation of •OH, which can more effectively promote the 4-NP degradation. For the rate-determining step of *PAP to *HQ, the reaction energy barrier of **TTCOF-Co** is 1.87 eV, which is much lower than that of **TTCOF-Ni** and **TTCOF-Cu**. Thus, **TTCOF-Co** has the highest 4-NP degradation activity and can efficiently complete the 4-NP electro-degradation process.

■ CONCLUSIONS

In summary, a series of porphyrin-based COFs (**TTCOF-M, M = Co, Ni,** and **Cu**) with tunable active sites have been applied as model catalysts to explore the photoassisted hybrid CO_2 electrocatalytic full reaction, during which the catalysts can simultaneously accomplish efficient CO_2 electroreduction and 4-NP mineralization. The effects of various model catalysts have been intensively studied from typical tandem electro-reactions to extended photoassisted ones. Notably, **TTCOF-Co** enables achieving the cathodic reduction efficiency increasing from 90 to 96% (−0.7 V) after illumination and simultaneously 5 times shortened reaction time with a 4-NP degradation efficiency of ∼99%. Obviously, the 4-NP mineralization rate was calculated to be ∼93.51% with a ∼30.27 mmol/g/h CO_2 production rate. Moreover, a rarely investigated mechanism relating to the 4-NP electro-degradation has been intensively studied and verified by various characterizations. This is the first case of COF-based electrocatalysts for photoassisted CO_2 electroreduction coupling pollutant degradation, which would pave a new way for the exploration of porous crystalline materials in the extended photoassisted CO_2RR coupling techniques to potentially address environmental issues.

■ EXPERIMENTAL SECTION

Synthesis of Tetrakis(4-aminophenyl)-porphinato Cobalt (TAPP-Co). TAPP (405 mg, 0.6 mmol) and $Co(OAc)_2{\cdot}4H_2O$ (598 mg, 2.4 mmol) were added in a 500 mL three-neck round-bottomed flask. After purification with high-purity nitrogen gas three times, the mixed solution of methanol (40 mL), chloroform (180 mL), and DMF (60 mL) was added. The mixture was heated at 80 °C under stirring and a nitrogen atmosphere for 24 h. After cooling to room temperature, the precipitate was filtered and washed with water three times. The product was dried under vacuum overnight at 80 °C.

Syntheses of Tetrakis(4-aminophenyl)-porphinato Nickel (TAPP-Ni) and Copper (TAPP-Cu). The syntheses of TAPP-Ni and TAPP-Cu were similar to that of TAPP-Co except that $Co(OAc)_2{\cdot}4H_2O$ was replaced by $Ni(OAc)_2{\cdot}4H_2O$ (597 mg, 2.4 mmol) and $Cu(OAc)_2{\cdot}2H_2O$ (479 mg, 2.4 mmol).

Synthesis of TTCOF-Co. The synthesis method of TTCOF-Co follows previously reported procedures. TAPP-Co (14.7 mg, 0.02 mmol), TTF-4CHO (12.5 mg, 0.02 mmol), mesitylene (0.5 mL), 1,

https://doi.org/10.1021/acs.chemmater.2c02962
Chem. Mater. 2022, 34, 10752−10760

4-dioxane (0.5 mL), and 6 M aqueous acetic acid (0.3 mL) were mixed in a Pyrex tube (o.d × length, 19 × 65 mm). After sonication for about 15 min, the tube was flash-frozen at 77 K (liquid N2 bath) and degassed to achieve an internal pressure of ∼100 mTorr. After the temperature recovers to room temperature, the mixture was heated at 120 °C for 120 h. After filtration, the wet sample was transferred to a Soxhlet extractor and washed with THF (24 h). Finally, the product was evacuated at 120 °C under dynamic vacuum overnight to yield the activated sample.

Synthesis of TTCOF-Ni and TTCOF-Cu. The syntheses of TTCOF-Ni and TAPP-Cu were carried out following the same protocols as that of TTCOF-Co, during which TAPP-Co was replaced by TAPP-Ni (14.7 mg, 0.02 mmol) and TAPP-Cu (14.8 mg, 0.02 mmol), respectively.

Photoassisted CO_2 Electroreduction Coupling Pollutant Degradation. The electrolysis tests of the catalyst were carried out in a H-type cell at selected potentials to determine the CO_2 reduction activities and the 4-NP degradation process. In order to determine the performance of both ends, TTCOF-M (M = Co, Ni, and Cu) were packaged in cells and tested in the three-electrode electrochemical H-type cell with the CO_2-saturated 0.5 M $KHCO_3$ solution (pH = 7.2) or Ar-saturated 0.5 M $KHCO_3$ solution (pH = 8.8) (25 mL) as the cathode electrolyte and the mixed solution (25 mL) of 0.1 M Na_2SO_4, 0.5 g L^{-1} PMS, and 2 mg L^{-1} 4-NP as the anode electrolyte. In this work, all potentials were measured using the Ag/AgCl electrode as the reference electrode and the results are reported relative to the reversible hydrogen electrode (RHE) based on the Nernst equation: E (vs RHE) = E (vs Ag/AgCl) + 0.197 V + 0.059 × pH. The sealed carbon paper coated with the catalyst on both sides is used as the working electrode. Chronoamperometry was performed using an electrochemical workstation (CHI660E) with a standard three-electrode system at room temperature. The electrolyte solution was collected from the cathode chambers to analyze the liquid products and characterized by ^{1}H NMR, in which 0.5 mL of the electrolyte was mixed with 0.1 mL of D_2O. Similarly, the electrolyte solution was collected from the anode chamber and the absorbance of 4-NP in the liquid was determined by an ultraviolet spectrophotometer (UH5300). The concentration of 4-NP was calculated according to Lambert−Beer's law, and the degradation efficiency was obtained. For the photoassisted co-electrolysis, a 300 W xenon arc lamp (light intensity, 400 mW cm^{-2}) with full light (wavelength, 200 to 1200 nm) was used as the light source with a similar distance of ∼10 cm to the related cathode and anode. The potential of the electrochemical degradation reaction was −0.7 V vs RHE under light irradiation.

■ ASSOCIATED CONTENT

Supporting Information

The Supporting Information is available free of charge at https://pubs.acs.org/doi/10.1021/acs.chemmater.2c02962.

Detailed information regarding the experimental procedures, characterization analysis, and DFT calculations (PDF)

■ AUTHOR INFORMATION

Corresponding Authors

Yifa Chen − *School of Chemistry, South China Normal University, Guangzhou 510006, P. R. China;* orcid.org/0000-0002-1718-6871; Email: chyf927821@163.com

Ya-Qian Lan − *Jiangsu Collaborative Innovation Centre of Biomedical Functional Materials, Jiangsu Key Laboratory of New Power Batteries, School of Chemistry and Materials Science, Nanjing Normal University, Nanjing 210023, P. R. China; School of Chemistry, South China Normal University, Guangzhou 510006, P. R. China;* orcid.org/0000-0002-2140-7980; Email: yqlan@m.scnu.edu.cn, yqlan@njnu.edu.cn

Authors

Huimin Ding − *Jiangsu Collaborative Innovation Centre of Biomedical Functional Materials, Jiangsu Key Laboratory of New Power Batteries, School of Chemistry and Materials Science, Nanjing Normal University, Nanjing 210023, P. R. China*

Yi-Rong Wang − *School of Chemistry, South China Normal University, Guangzhou 510006, P. R. China*

Ming Liu − *Jiangsu Collaborative Innovation Centre of Biomedical Functional Materials, Jiangsu Key Laboratory of New Power Batteries, School of Chemistry and Materials Science, Nanjing Normal University, Nanjing 210023, P. R. China*

Jing-Wen Shi − *Jiangsu Collaborative Innovation Centre of Biomedical Functional Materials, Jiangsu Key Laboratory of New Power Batteries, School of Chemistry and Materials Science, Nanjing Normal University, Nanjing 210023, P. R. China*

Tao-Yuan Yu − *Jiangsu Collaborative Innovation Centre of Biomedical Functional Materials, Jiangsu Key Laboratory of New Power Batteries, School of Chemistry and Materials Science, Nanjing Normal University, Nanjing 210023, P. R. China*

Yuan-Sheng Xia − *Jiangsu Collaborative Innovation Centre of Biomedical Functional Materials, Jiangsu Key Laboratory of New Power Batteries, School of Chemistry and Materials Science, Nanjing Normal University, Nanjing 210023, P. R. China*

Meng Lu − *School of Chemistry, South China Normal University, Guangzhou 510006, P. R. China*

Yi-Lu Yang − *School of Chemistry, South China Normal University, Guangzhou 510006, P. R. China*

Shun-Li Li − *School of Chemistry, South China Normal University, Guangzhou 510006, P. R. China*

Complete contact information is available at: https://pubs.acs.org/10.1021/acs.chemmater.2c02962

Author Contributions

Y.-Q.L., Y.C., and H.D. conceived the idea. H.D. designed the experiments, collected, and analyzed the data. Y.-R.W., M.L., J.-W.S., T.-Y.Y., Y.-S.X., M.L., and Y.-L.Y. assisted the experiments and characterizations. H.D. wrote the manuscript. All authors have approved the final version of the manuscript. H.D. and Y.-R.W. contributed equally to this work.

Notes

The authors declare no competing financial interest.

■ ACKNOWLEDGMENTS

This work was financially supported by the NSFC (Grants 22171139, 22225109, 21871141, 21871142, 21901122, and 22071109), the Priority Academic Program Development of Jiangsu Higher Education Institutions, and the Foundation of Jiangsu Collaborative Innovation Center of Biomedical Functional Materials.

■ REFERENCES

(1) Sousa, J. C. G.; Ribeiro, A. R.; Barbosa, M. O.; Pereira, M. F. R.; Silva, A. M. T. A review on environmental monitoring of water organic pollutants identified by EU guidelines. *J. Hazard. Mater.* **2018**, *344*, 146−162.

(2) Dinesh, M.; Roopan, S. M.; Selvaraj, C. I. Photocatalytic degradation of nitrophenol using biologically active Phyllanthus emblica seed extract. *J. Photochem. Photobiol., B* **2016**, *161*, 273−278.

(3) Mei, Q.; Sun, J.; Han, D.; Wei, B.; An, Z.; Wang, X.; Xie, J.; Zhan, J.; He, M. Sulfate and hydroxyl radicals-initiated degradation reaction on phenolic contaminants in the aqueous phase: Mechanisms, kinetics and toxicity assessment. *Chem. Eng. J.* **2019**, *373*, 668−676.

(4) Li, J.; Liang, Y.; Wu, S.; Zhang, Y.; Zhu, M.; Gao, E. A novel Zn metal organic framework for the detection of o-nitrophenol, m-nitrophenol, p−nitrophenol. *Inorg. Chem. Commun.* **2022**, *143*, No. 109724.

(5) Abazari, R.; Mahjoub, A. R.; Salehi, G. Preparation of amine functionalized g-C_3N_4@(H/S)MOF NCs with visible light photocatalytic characteristic for 4-nitrophenol degradation from aqueous solution. *J. Hazard. Mater.* **2019**, *365*, 921−931.

(6) Zhang, W.; Li, G.; Wang, W.; Qin, Y.; An, T.; Xiao, X.; Choi, W. Enhanced photocatalytic mechanism of Ag_3PO_4 nano-sheets using MS_2 (M = Mo, W)/rGO hybrids as co-catalysts for 4-nitrophenol degradation in water. *Appl. Catal., B* **2018**, *232*, 11−18.

(7) Ma, Z.; Guan, Y.; Liu, H. Synthesis and characterization of micron-sized monodisperse superparamagnetic polymer particles with amino groups. *J. Polym. Sci., Part A: Polm. Chem.* **2005**, *43*, 3433−3439.

(8) Chen, Q.; Ma, C.; Duan, W.; Lang, D.; Pan, B. Coupling adsorption and degradation in p-nitrophenol removal by biochars. *J. Cleaner Prod.* **2020**, *271*, No. 122550.

(9) Luo, X.; Liang, H.; Qu, F.; Ding, A.; Cheng, X.; Tang, C. Y.; Li, G. Free-standing hierarchical alpha-MnO_2@CuO membrane for catalytic filtration degradation of organic pollutants. *Chemosphere* **2018**, *200*, 237−247.

(10) Bose, S.; Kumar, P. S.; Vo, D.-V. N.; Rajamohan, N.; Saravanan, R. Microbial degradation of recalcitrant pesticides. *Environ. Chem. Lett.* **2021**, *19*, 3209−3228.

(11) Chauhan, R.; Dinesh, G. K.; Alawa, B.; Chakma, S. A critical analysis of sono-hybrid advanced oxidation process of ferrioxalate system for degradation of recalcitrant pollutants. *Chemosphere* **2021**, *277*, No. 130324.

(12) Tian, L.; Zhu, M.; Zhang, L.-S.; Zhou, L.-J.; Fan, J.-P.; Wu, D.-S.; Zou, J.-P. New insights on the role of NaCl electrolyte for degradation of organic pollutants in the system of electrocatalysis coupled with advanced oxidation processes. *J. Environ. Chem. Eng.* **2022**, *10*, No. 107414.

(13) Peng, J.; Zhang, W.; Wang, J.; Li, L.; Lai, W.; Yang, Q.; Zhang, B.; Li, X.; Du, Y.; Liu, H.; Wang, J.; Cheng, Z.; Wang, L.; Wang, S.; Wang, J.; Chou, S.; Liu, H.; Dou, S. Processing Rusty Metals into Versatile Prussian Blue for Sustainable Energy Storage. *Adv. Energy Mater.* **2021**, *11*, No. 2102356.

(14) Chen, M.; Zhang, Y.; Xing, G.; Chou, S.-L.; Tang, Y. Electrochemical energy storage devices working in extreme conditions. *Energy Environ. Sci.* **2021**, *14*, 3323−3351.

(15) Wang, J.; Hu, H.; Lu, S.; Hu, J.; Zhu, H.; Duan, F.; Du, M. Conductive metal and covalent organic frameworks for electrocatalysis: design principles, recent progress and perspective. *Nanoscale* **2022**, *14*, 277−288.

(16) Tan, X.; Yu, C.; Ren, Y.; Cui, S.; Li, W.; Qiu, J. Recent advances in innovative strategies for the CO_2 electroreduction reaction. *Energy Environ. Sci.* **2021**, *14*, 765−780.

(17) Usman, M.; Humayun, M.; Garba, M. D.; Ullah, L.; Zeb, Z.; Helal, A.; Suliman, M. H.; Alfaifi, B. Y.; Iqbal, N.; Abdinejad, M.; Tahir, A. A.; Ullah, H. Electrochemical Reduction of CO_2: A Review of Cobalt Based Catalysts for Carbon Dioxide Conversion to Fuels. *Nanomaterials* **2021**, *11*, 2029.

(18) Liu, A.; Gao, M.; Ren, X.; Meng, F.; Yang, Y.; Gao, L.; Yang, Q.; Ma, T. Current progress in electrocatalytic carbon dioxide reduction to fuels on heterogeneous catalysts. *J. Mater. Chem. A* **2020**, *8*, 3541−3562.

(19) Yang, R.-X.; Wang, Y.-R.; Gao, G.-K.; Chen, L.; Chen, Y.; Li, S.-L.; Lan, Y.-Q. Self-Assembly of Hydroxyl Metal−Organic Polyhedra and Polymer into Cu-Based Hollow Spheres for Product-Selective CO_2 electroreduction. *Small Struct.* **2021**, *2*, No. 2100012.

(20) Yang, Y.-L.; Wang, Y.-R.; Gao, G.-K.; Liu, M.; Miao, C.; Li, L.-Y.; Cheng, W.; Zhao, Z.-Y.; Chen, Y.; Xin, Z.; Li, S.-L.; Li, D.-S.; Lan, Y.-Q. Self-assembly of single metal sites embedded covalent organic frameworks into multi-dimensional nanostructures for efficient CO_2 electroreduction. *Chin. Chem. Lett.* **2022**, *33*, 1439−1444.

(21) Wang, P.; Yang, H.; Tang, C.; Wu, Y.; Zheng, Y.; Cheng, T.; Davey, K.; Huang, X.; Qiao, S.-Z. Boosting electrocatalytic CO2−to−ethanol production via asymmetric C−C coupling. *Nat. Commun.* **2022**, *13*, 3754.

(22) Tahir, M.; Pan, L.; Idrees, F.; Zhang, X.; Wang, L.; Zou, J.-J.; Wang, Z. L. Electrocatalytic oxygen evolution reaction for energy conversion and storage: A comprehensive review. *Nano Energy* **2017**, *37*, 136−157.

(23) Zeng, F.; Mebrahtu, C.; Liao, L.; Beine, A.; Palkovits, R. Stability and deactivation of OER electrocatalysts. *J. Energy Chem.* **2022**, *69*, 301−329.

(24) Zhang, Y.-C.; Han, C.; Gao, J.; Pan, L.; Wu, J.; Zhu, X.-D.; Zou, J.-J. NiCo-Based Electrocatalysts for the Alkaline Oxygen Evolution Reaction: A Review. *ACS Catal.* **2021**, *11*, 12485−12509.

(25) Zhu, W.; Huang, Z.; Zhao, M.; Huang, R.; Wang, Z.; Liang, H. Hydrogen production by electrocatalysis using the reaction of acidic oxygen evolution: a review. *Environ. Chem. Lett.* **2022**, DOI: 10.1007/s10311-022-01454-5.

(26) Wang, H. F.; Chen, L.; Pang, H.; Kaskel, S.; Xu, Q. MOF-derived electrocatalysts for oxygen reduction, oxygen evolution and hydrogen evolution reactions. *Chem. Soc. Rev.* **2020**, *49*, 1414−1448.

(27) Ma, Y.; Wang, J.; Yu, J.; Zhou, J.; Zhou, X.; Li, H.; He, Z.; Long, H.; Wang, Y.; Lu, P.; Yin, J.; Sun, H.; Zhang, Z.; Fan, Z. Surface modification of metal materials for high-performance electrocatalytic carbon dioxide reduction. *Matter* **2021**, *4*, 888−926.

(28) Wang, J.; Huang, X.; Xi, S.; Xu, H.; Wang, X. Axial Modification of Cobalt Complexes on Heterogeneous Surface with Enhanced Electron Transfer for Carbon Dioxide Reduction. *Angew. Chem., Int. Ed.* **2020**, *59*, 19162−19167.

(29) Zhou, X.; Dong, J.; Zhu, Y.; Liu, L.; Jiao, Y.; Li, H.; Han, Y.; Davey, K.; Xu, Q.; Zheng, Y.; Qiao, S.-Z. Molecular Scalpel to Chemically Cleave Metal−Organic Frameworks for Induced Phase Transition. *J. Am. Chem. Soc.* **2021**, *143*, 6681−6690.

(30) Tang, J.; Weiss, E.; Shao, Z. Advances in cutting-edge electrode engineering toward CO2 electrolysis at high current density and selectivity: A mini-review. *Carbon Neutralization* **2022**, *1*, 140−158.

(31) Salvatore, D. A.; Gabardo, C. M.; Reyes, A.; O'Brien, C. P.; Holdcroft, S.; Pintauro, P.; Bahar, B.; Hickner, M.; Bae, C.; Sinton, D.; Sargent, E. H.; Berlinguette, C. P. Designing anion exchange membranes for CO_2 electrolysers. *Nat. Energy* **2021**, *6*, 339−348.

(32) Fujinuma, N.; Ikoma, A.; Lofland, S. E. Highly Efficient Electrochemical CO_2 Reduction Reaction to CO with One-Pot Synthesized Co-Pyridine-Derived Catalyst Incorporated in a Nafion-Based Membrane Electrode Assembly. *Adv. Energy Mater.* **2020**, *10*, No. 2001645.

(33) Wang, Q.; Wang, X.; Wu, C.; Cheng, Y.; Sun, Q.; Yu, H. Enhanced electroreduction of CO_2 and simultaneous degradation of organic pollutants using a Sn-based carbon nanotubes/carbon black hybrid gas diffusion cathode. *J. CO2 Util.* **2018**, *26*, 425−433.

(34) Zhu, M.; Zhang, L.; Liu, S.; Wang, D.; Qin, Y.; Chen, Y.; Dai, W.; Wang, Y.; Xing, Q.; Zou, J. Degradation of 4-nitrophenol by electrocatalysis and advanced oxidation processes using Co_3O_4@C anode coupled with simultaneous CO_2 reduction via SnO_2/CC cathode. *Chin. Chem. Lett.* **2020**, *31*, 1961−1965.

(35) Zou, J. P.; Chen, Y.; Liu, S. S.; Xing, Q. J.; Dong, W. H.; Luo, X. B.; Dai, W. L.; Xiao, X.; Luo, J. M.; Crittenden, J. Electrochemical oxidation and advanced oxidation processes using a 3D hexagonal Co_3O_4 array anode for 4-nitrophenol decomposition coupled with simultaneous CO_2 conversion to liquid fuels via a flower-like CuO cathode. *Water Res.* **2019**, *150*, 330−339.

(36) Ma, J.; Ren, J.; Jia, Y.; Wu, Z.; Chen, L.; Haugen, N. O.; Huang, H.; Liu, Y. High efficiency bi-harvesting light/vibration energy using piezoelectric zinc oxide nanorods for dye decomposition. *Nano Energy* **2019**, *62*, 376−383.

(37) Yek, P. N. Y.; Peng, W.; Wong, C. C.; Liew, R. K.; Ho, Y. L.; Wan Mahari, W. A.; Azwar, E.; Yuan, T. Q.; Tabatabaei, M.; Aghbashlo, M.; Sonne, C.; Lam, S. S. Engineered biochar via microwave CO_2 and steam pyrolysis to treat carcinogenic Congo red dye. *J. Hazard. Mater.* **2020**, *395*, No. 122636.
(38) Lu, M.; Zhang, M.; Liu, C. G.; Liu, J.; Shang, L. J.; Wang, M.; Chang, J. N.; Li, S. L.; Lan, Y. Q. Stable Dioxin-Linked Metallophthalocyanine Covalent Organic Frameworks (COFs) as Photo-Coupled Electrocatalysts for CO_2 Reduction. *Angew. Chem., Int. Ed.* **2021**, *60*, 4864−4871.
(39) Fang, H.; Han, Y.; Feng, X.; Ji, W.; Au, C.-T. S-scheme heterojunction g-C_3N_4/Ag/AgNCO for efficient tetracycline removal in a photo-assisted peroxymonosulfate system. *Sep. Purif. Technol.* **2022**, *296*, No. 121210.
(40) Rao, K. R.; Pishgar, S.; Strain, J.; Kumar, B.; Atla, V.; Kumari, S.; Spurgeon, J. M. Photoelectrochemical reduction of CO_2 to HCOOH on silicon photocathodes with reduced SnO_2 porous nanowire catalysts. *J. Mater. Chem. A* **2018**, *6*, 1736−1742.
(41) Zhao, E.; Du, K.; Yin, P. F.; Ran, J.; Mao, J.; Ling, T.; Qiao, S. Z. Advancing Photoelectrochemical Energy Conversion through Atomic Design of Catalysts. *Adv. Sci.* **2021**, *9*, No. 2104363.
(42) Qiao, F.; Sun, K.; Chu, H.; Wang, J.; Xie, Y.; Chen, L.; Yan, T. Design strategies of ZnO heterojunction arrays towards effective photovoltaic applications. *Battery Energy.* **2022**, *1*, No. 20210008.
(43) Zhao, X.; Pachfule, P.; Thomas, A. Covalent organic frameworks (COFs) for electrochemical applications. *Chem. Soc. Rev.* **2021**, *50*, 6871−6913.
(44) Guan, Q.; Zhou, L. L.; Dong, Y. B. Metalated covalent organic frameworks: from synthetic strategies to diverse applications. *Chem. Soc. Rev.* **2022**, *51*, 6307.
(45) Mallakpour, S.; Azadi, E.; Hussain, C. M. Emerging new-generation hybrids based on covalent organic frameworks for industrial applications. *New J. Chem.* **2021**, *45*, 7014−7046.
(46) Lin, S.; Diercks Christian, S.; Zhang, Y.-B.; Kornienko, N.; Nichols Eva, M.; Zhao, Y.; Paris Aubrey, R.; Kim, D.; Yang, P.; Yaghi Omar, M.; Chang Christopher, J. Covalent organic frameworks comprising cobalt porphyrins for catalytic CO_2 reduction in water. *Science* **2015**, *349*, 1208−1213.
(47) Wang, J.; Zhuang, S. Covalent organic frameworks (COFs) for environmental applications. *Coord. Chem. Rev.* **2019**, *400*, No. 213046.
(48) Chen, M.; Li, H.; Liu, C.; Liu, J.; Feng, Y.; Wee, A. G. H.; Zhang, B. Porphyrin- and porphyrinoid-based covalent organic frameworks (COFs): From design, synthesis to applications. *Coord. Chem. Rev.* **2021**, *435*, No. 213778.
(49) Yuan, J.; Chen, S.; Zhang, Y.; Li, R.; Zhang, J.; Peng, T. Structural Regulation of Coupled Phthalocyanine-Porphyrin Covalent Organic Frameworks to Highly Active and Selective Electrocatalytic CO_2 Reduction. *Adv. Mater.* **2022**, *34*, No. e2203139.
(50) Wu, Q.; Xie, R.-K.; Mao, M.-J.; Chai, G.-L.; Yi, J.-D.; Zhao, S.-S.; Huang, Y.-B.; Cao, R. Integration of Strong Electron Transporter Tetrathiafulvalene into Metalloporphyrin-Based Covalent Organic Framework for Highly Efficient Electroreduction of CO_2. *ACS Energy Lett.* **2020**, *5*, 1005−1012.
(51) Chi, S.-Y.; Chen, Q.; Zhao, S.-S.; Si, D.-H.; Wu, Q.-J.; Huang, Y.-B.; Cao, R. Three-dimensional porphyrinic covalent organic frameworks for highly efficient electroreduction of carbon dioxide. *J. Mater. Chem. A* **2022**, *10*, 4653−4659.
(52) Huang, S.; Chen, K.; Li, T.-T. Porphyrin and phthalocyanine based covalent organic frameworks for electrocatalysis. *Coord. Chem. Rev.* **2022**, *464*, No. 214563.
(53) Chen, Y.; Li, W.; Wang, X.-H.; Gao, R.-Z.; Tang, A.-N.; Kong, D.-M. Green synthesis of covalent organic frameworks based on reaction media. *Mater. Chem. Front.* **2021**, *5*, 1253−1267.
(54) Vitaku, E.; Dichtel, W. R. Synthesis of 2D Imine-Linked Covalent Organic Frameworks through Formal Transimination Reactions. *J. Am. Chem. Soc.* **2017**, *139*, 12911−12914.
(55) Lu, M.; Liu, J.; Li, Q.; Zhang, M.; Liu, M.; Wang, J. L.; Yuan, D. Q.; Lan, Y. Q. Rational Design of Crystalline Covalent Organic Frameworks for Efficient CO_2 Photoreduction with H_2O. *Angew. Chem., Int. Ed.* **2019**, *58*, 12392−12397.
(56) Li, Y.; Zhang, J.; Zuo, K.; Li, Z.; Wang, Y.; Hu, H.; Zeng, C.; Xu, H.; Wang, B.; Gao, Y. Covalent Organic Frameworks for Simultaneous CO2 Capture and Selective Catalytic Transformation. *Catalysts* **2021**, *11*, 1133.
(57) Mi, Z.; Zhou, T.; Weng, W.; Unruangsri, J.; Hu, K.; Yang, W.; Wang, C.; Zhang, K. A. I.; Guo, J. Covalent Organic Frameworks Enabling Site Isolation of Viologen-Derived Electron-Transfer Mediators for Stable Photocatalytic Hydrogen Evolution. *Angew. Chem., Int. Ed.* **2021**, *60*, 9642−9649.
(58) Tang, Y.-J.; Zhu, H.-J.; Dong, L.-Z.; Zhang, A. M.; Li, S.-L.; Liu, J.; Lan, Y.-Q. Solid-phase hot-pressing of POMs-ZIFs precursor and derived phosphide for overall water splitting. *Appl. Catal., B* **2019**, *245*, 528−535.
(59) Wang, Y.-R.; Yang, R.-X.; Chen, Y.; Gao, G.-K.; Wang, Y.-J.; Li, S.-L.; Lan, Y.-Q. Chloroplast-like porous bismuth-based core−shell structure for high energy efficiency CO_2 electroreduction. *Sci. Bull.* **2020**, *65*, 1635−1642.
(60) Wang, S.; Gao, S.; Tian, J.; Wang, Q.; Wang, T.; Hao, X.; Cui, F. A stable and easily prepared copper oxide catalyst for degradation of organic pollutants by peroxymonosulfate activation. *J. Hazard. Mater.* **2020**, *387*, No. 121995.
(61) Wang, L.; Lan, X.; Peng, W.; Wang, Z. Uncertainty and misinterpretation over identification, quantification and transformation of reactive species generated in catalytic oxidation processes: A review. *J. Hazard. Mater.* **2021**, *408*, No. 124436.
(62) Song, R.; Chi, H.; Ma, Q.; Li, D.; Wang, X.; Gao, W.; Wang, H.; Wang, X.; Li, Z.; Li, C. Highly Efficient Degradation of Persistent Pollutants with 3D Nanocone TiO_2-Based Photoelectrocatalysis. *J. Am. Chem. Soc.* **2021**, *143*, 13664−13674.
(63) Xu, Z.; Gao, Y.; Gu, H.; Gu, S.; Xiong, M.; Zhang, D.; Qi, R.; Chen, W. Novel Fe^0-C/S(IV) system: Toward the interaction between Fe^0-C internal electrolysis and sulfite for p-nitrophenol degradation. *Sep. Purif. Technol.* **2021**, *268*, No. 118615.
(64) Grimme, S.; Antony, J.; Ehrlich, S.; Krieg, H. A consistent and accurate ab initio parametrization of density functional dispersion correction (DFT-D) for the 94 elements H-Pu. *J. Chem. Phys.* **2010**, *132*, 154104.
(65) Perdew, J. P.; Chevary, J. A.; Vosko, S. H.; Jackson, K. A.; Pederson, M. R.; Singh, D. J.; Fiolhais, C. Atoms, molecules, solids, and surfaces: Applications of the generalized gradient approximation for exchange and correlation. *Phys. Rev. B* **1992**, *46*, 6671−6687.
(66) Blochl, P. E. Projector augmented-wave method. *Phys. Rev. B* **1994**, *50*, 17953−17979.

https://doi.org/10.1021/acs.chemmater.2c02962
Chem. Mater. 2022, 34, 10752−10760